Europe PMC Funders Group
Author Manuscript
Nat Mater. Author manuscript; available in PMC 2017 July 03.

Published in final edited form as:
Nat Mater. 2016 June ; 15(6): 640–646. doi:10.1038/nmat4588.

Coordination polymer structure and revisited hydrogen evolution catalytic mechanism for amorphous molybdenum sulfide

Phong D. Tran[a,b,c,*], **Thu V. Tran**[d], **Maylis Orio**[e], **Stephane Torelli**[f], **Quang Duc Truong**[g], **Keiichiro Nayuki**[h], **Yoshikazu Sasaki**[h], **Sing Yang Chiam**[i], **Ren Yi**[i], **Itaru Honma**[g], **James Barber**[b,k], and **Vincent Artero**[f,*]

[a]Energy Research Institute, Nanyang Technological University, 50 Nanyang Drive, Singapore 637553

[b]Solar Fuel Laboratory, School of Materials Science & Engineering, Nanyang Technological University, 50 Nanyang Avenue, Singapore 639798

[c]Department of Advanced Materials Science and Nanotechnology, University of Science and Technology of Hanoi, 18 Hoang Quoc Viet, Hanoi, Vietnam

[d]Electronics-Inspired Interdisplinary Research Institute, Toyohashi University of Technology, 1-1 Hibarigaoka, Tempaku, Toyohashi 441-8580 Japan

[e]ISM2 Institut des Sciences Moléculaires de Marseille ; Aix Marseille Univ. ; CNRS ; Campus Scientifique de St Jérôme, 13020 Marseille, France

[f]Laboratoire de Chimie et Biologie des Métaux ; Univ. Grenoble Alpes ; CNRS ; CEA; 17 rue des Martyrs, 38054 Grenoble, France

[g]Institute of Multidisciplinary Research for Advanced Materials, Tohoku University, 2-1-1, Katahira, Aobaku, Sendai 980-8577, Japan

[h]Field Solution Division, JEOL Ltd., 1156, Nakagami, Akishima, Tokyo 196-0022, Japan

[i]Institute of Materials Research and Engineering, A*STAR (Agency for Science, Technology and Research), 3 Research Link, Singapore 117602

[k]Department of Life Sciences, Imperial College London, SW7 2AZ London, UK

Abstract

Molybdenum sulfides are very attractive noble-metal free electrocatalysts for the hydrogen evolution reaction (HER) from water. Atomic structure and identity of the catalytically active sites have been well established for crystalline molybdenum disulfide (*c*-MoS_2) but not for amorphous molybdenum sulfide (*a*-MoS_x) which displays significantly higher HER activity compared to its

* tran-dinh.phong@usth.edu.vn; vincent.artero@cea.fr.

Author contributions

P.D.T. and VA designed research, performed material synthesis and electrochemical studies. T.V.T. performed resonant Raman analysis. Q.D.T, K.N., Y.S. and I.H. performed and analysed STEM studies. S.Y.C. and R.Y. performed XPS studies. S.T. and V.A. performed and analyzed EPR studies. M.O performed DFT calculation. P.D.T, V.A. and J.B. wrote the paper.

Europe PMC Funders Author Manuscripts
Europe PMC Funders Author Manuscripts

Europe PMC Funders Author Manuscripts

crystalline counterpart. Here we show that HER–active *a*-MoS_x, prepared either as nanoparticles or as films, is a molecular–based coordination polymer consisting of discrete $[Mo_3S_{13}]^{2-}$ building blocks. Of the three terminal disulfide (S_2^{2-}) ligands within these clusters, two are shared to form the polymer chain. The third one remains free and generates molybdenum hydride moieties as the active site under H_2 evolution conditions. Such a molecular structure therefore provides a basis for revisiting the mechanism of *a*-MoS_x catalytic activity, as well as explaining some of its special properties such as reductive activation and corrosion. Our findings open up new avenues for the rational optimisation of this HER electrocatalyst as an alternative to platinum.

Scalable renewable hydrogen production *via* solar-driven water splitting employing a viable and cost-effective photoelectrochemical cell is a potential technology to address the global demand for renewable energy.1 To this end, several key challenges have been identified, including the search for efficient electrocatalysts based on earth`s abundant elements for the oxygen evolution reaction (OER) and the hydrogen evolution reaction (HER). During the last decade, significant advances have been achieved to identify HER electrocatalysts alternative to platinum and based on transition metals such as Fe,4 Ni,2–4 Co,4,5 Mo6–14 or W15,16. In particular crystalline molybdenum disulfide (*c*-MoS_2),6–9 amorphous molybdenum sulfide (*a*-MoS_x),10,11,14 and molybdenum sulfido clusters such as $[Mo_3S_4]^{4+}$ (ref 12), $[Mo_3S_{13}]^{2-}$ (ref 13) or $[Mo_2S_{12}]^{2-}$ (ref 17) have recently gained attention thanks to their scalable preparation methods, attractive catalytic activities and robustness, as well as their capability to be integrated in H_2-evolving photocathodes.18–22 In the case of *c*-MoS_2 (Fig. 1), edge-planes are responsible for HER activity while basal-planes are inactive.6,23 Edge-planes display Mo sites stabilized by disulfide ligands,24 but both the evolution of these motifs under turnover conditions and the catalytic HER mechanism remain unclear.23,25 Even less is known regarding the structure and catalytic mechanism of *a*-MoS_x despite its activity is higher than c-MoS_2. Indeed, no comprehensive structural insights are available for *a*-MoS_x, which stands as a critical obstacle for understanding its catalytic functions. In this study, we combined spectroscopic and electrochemical techniques with quantum chemistry to investigate the structure and reactivity of *a*-MoS_x.

A coordination polymer based on $[Mo_3S_{13}]^{2-}$ clusters

Belanger and coll.26 and Hu and coll.14 demonstrated electrodeposition of *a*-MoS_x as a thin film on conducting electrodes employing a solution of tetrathiomolybdate ($[MoS_4]^{2-}$). In pH 7 phosphate buffer solution, the electrochemical oxidation of $[MoS_4]^{2-}$ resulting in deposition of *a*-MoS_x has an onset potential of ~0.15 V *vs.* NHE (Methods section and Supplementary Fig. S1). Thin films (~40 nm) with good conductivity are obtained.11,26 Figure 2a (*red trace*) shows the resonance Raman spectrum of an *a*-MoS_x film deposited on a fluorine-doped tin oxide (FTO) electrode at 0.2 V *vs.* NHE. Remarkably, the *a*-MoS_x material has identical Raman signatures to those recently reported for isolated $[Mo_3S_{13}](NH_4)_2$ clusters (Fig. 1 and Supplementary Fig. S2).13 Vibration of bridging/shared disulfide ($\bar{\nu}(S\text{-}S)_{br/sh}$) and terminal disulfide ($\bar{\nu}(S\text{-}S)_t$) were found at 555 and 525 cm^{-1}, respectively. Molybdenum sulfide bonds were found at $\bar{\nu}$(Mo-S) of 382-284 cm^{-1} while the $\nu(Mo_3\text{-}\mu_3S)$ vibration was detected at 450 cm^{-1}.

Europe PMC Funders Author Manuscripts

Europe PMC Funders Author Manuscripts

Similar signatures were also obtained for *a*-MoS_x thin films and $[Mo_3S_{13}](NH_4)_2$ clusters using X-ray photoelectron spectroscopy (XPS, Fig 2b and 2c and Supplementary Information). Irrespective of the oxidation potential applied during electrodeposition, *a*-MoS_x films have identical Raman and XPS signatures. This also applies to *a*-MoS_x nanoparticles synthesized from aqueous $[MoS_4]^{2-}$ solution *via* chemical oxidation (Methods section and Supplementary Figs. S3 and S4). We thus conclude that *a*-MoS_x nanoparticles and thin films have identical molecular structures. Elemental analysis performed on the as-prepared *a*-MoS_x nanoparticles indicated that the mass fractions within the material are 36 ± 5 % for Mo and 50 ± 5 % for S. Similar Mo:S mass ratios have been obtained for *a*-MoS_x films electrodeposited on FTO electrodes and further dissolved in concentrated HNO_3 prior to analysis. Such a composition does not reflect the previously proposed MoS_3 composition but rather a Mo:S ratio of 4 and the presence of other elements (mainly oxygen, see below) accounting for 5-15 % of the mass. Interestingly, similar Mo:S mass ratios were found for *a*-MoS_x particles synthesized according to the procedure described by Jaramillo et al.11 We note that a MoS_4X (with X accounting for 14% of the mass) average composition would be in good agreement with the 22% Mo and 78% S molar composition11 determined from XPS data for such as synthesized amorphous molybdenum sulfide particles. The above analysis also shows that *a*-MoS_x is significantly distinct in composition from the recently reported *a*-MoS_xCl_y material.42

We employed the aberration-corrected scanning transmission electron microscopy (STEM) using high-angle annular dark field (HAADF) detector to determine the atomic structure of *a*-MoS_x (Supplementary Information). Figure 3 shows HAADF-STEM images of sub-monolayer of *a*-MoS_x on graphite flake, in which the brightness contrast provides evidence for the position of Mo atoms of *a*-MoS_x. The low-magnification image (Fig. 3a) shows crowded bright spots, indicating the presence of well-separated sub-nano and nano-sized particles without any specific shape (Supplementary Fig. S5a) and composed of 6 to 60 Mo atoms (mean value: 28 ±14 atoms). The building units of these particles are identified to be $[Mo_3]$ clusters wherein the Mo-Mo distance is 2.1 ± 0.7 Å, (Supplementary Fig. S5b). This distance is in agreement with that determined for Mo-Mo bonds (2.72 Å) within $[Mo_3S_{13}]^{2-}$ clusters.27 The $[Mo_3]$ clusters arrange in unfolded one-dimensional chains or two-dimensional networks reticulated through clusters which do not have free terminal disulfide group (Figs. 3b and 3c). To further support these observations, we successfully carried out the extrusion and isolation of $[Mo_3S_{13}]^2$ clusters from *a*-MoS_x following the procedure described by Muller *et al.*28 (Methods section and Supplementary Information).

The presence of defect Mo^V=O sites in various protonation states within grown *a*-MoS_x material is evidenced by spectroscopic analyses. XPS Mo $3d_{5/2}$ analysis shows minor species having binding energy of 230.76 eV (Fig. 2c) being assignable to Mo=O defect centers by comparison with energies reported for molybdenum oxysulfides (MoO_xS_y) (Mo $3d_{5/2}$: 231.10 eV, ref 29). The presence of MoO_3, characterised by high binding energy (Mo $3d_{5/2}$ ~232.50 eV), is excluded.30,31 Resonance Raman analysis (Fig. 2a, insert) shows vibration bands in the 800-950 cm^{-1} region characteristic of Mo=O motifs.32–34 Electron paramagnetic resonance (EPR) analysis, performed on as prepared *a*-MoS_x suspended in frozen pH 7 phosphate buffer, shows a complex spectrum (Fig. 2d, *red trace*). It can be analysed as a combination of two broad signals ($g^a\perp$ = 1.92 and $g^a_{//}$ = 1.86; g^b_1 = 2.05, g^b_2

Europe PMC Funders Author Manuscripts

Europe PMC Funders Author Manuscripts

= 2.01 and g^b_3 = 1.97) involving Mo^V species plus a thin signal at g = 2.003 corresponding to a non-metallic radical species. The broad signal with quasi–axial symmetry ($g^a \perp$ = 1.92 and $g^a_{//}$ = 1.86) is well documented in MoS_x materials and corresponds to Mo^V=O species (ref 35 and refs 8, 13, 15 19 therein). The rhombic signal (g^b_1 = 2.05, g^b_2 = 2.01 and g^b_3 = 1.97) also corresponds to Mo^V species, but coordinated to sulfur-based ligands (likely S_2^{2-}, although S^{2-} and HS^- cannot be excluded) as previously established for *c*-MoS_x materials.35 To understand the origin of the remaining signal, DFT calculations were performed on truncated models (Supplementary Fig. S9) of the [Mo_3] clusters reproducing the various coordination spheres of Mo shown in Fig. 1. The charge of the models was set as formally containing two Mo^{IV} and one Mo^V centers (this corresponding to [Mo_3] clusters with S = 1/2). Mono-protonated models were also considered. For each model, geometry optimization was first conducted followed by broken symmetry single point calculation to determine the electronic and magnetic properties. We found only one model (**A** cluster) with magnetic properties resembling the one of an organic radical with g values close to 2.003. The structure of **A** cluster derives from the above mentioned Mo^V=O species through protonation on a shared disulfide ligand. Such a protonation results in complete spin redistribution within the **A** cluster as shown in Supplementary Fig. S9 and Tables S1 and S2.

All above results are consistent with *a*-MoS_x being a coordination polymer based on $[Mo_3S_{13}]^{2-}$ clusters as building blocks sharing two of their three terminal disulfide groups (Fig. 1).

Electrochemical properties of *a*-MoS_x catalyst: catalytic pre-peaks

Potential polarization curves recorded employing an *a*-MoS_x electrode in different pH electrolyte solutions are shown in Fig. 4a. In pH 7 phosphate solution, two pre-catalytic reduction events at peak potentials E_{peak1} = –0.44 V and E_{peak2} = –0.54 V *vs.* NHE were observed prior to the catalytic hydrogen evolution wave (Fig. 4a, *insert*). Similar features were observed in more basic electrolyte solutions while in more acidic solutions the two pre-catalytic reduction events merged into one single pre-peak. At pH 0, this pre-catalytic peak was no longer observed. Such pre-peaks were only observed during the first cathodic polarization of freshly prepared *a*-MoS_x electrodes. Subsequent polarizations showed only the catalytic H_2 evolution wave (Supplementary Fig. S10). This indicates that the first cathodic polarization irreversibly transforms the *a*-MoS_x film into a novel material which is the actual HER catalyst. Plotting pre-catalytic peak potentials versus pH, we found that the first reduction event E_{peak1} was pH independent while the second event E_{peak2} had a dependence of 55 mV per pH unit (Fig. 4b). Thus, no proton is involved in the first reduction process while equal numbers of protons and electrons are involved during the second reduction event.

Analysis carried out on *a*-MoS_x films after being equilibrated at each pre-wave potential for 1h (Methods section) shows no derivation on Raman vibration signatures (Fig. 2a). This indicates that the disulfide ligands are not displaced at these potentials. Similar observation has been reported for the $[Mo_3S_{13}]^{2-}$ molecular catalyst13 and *a*-MoS_x.25 In other words, the pre-catalytic events are not relevant to the redox chemistry of the disulfide ligands. We thus hypothesize that the pre-waves correspond to the reduction of structural defects such as

Europe PMC Funders Author Manuscripts

Europe PMC Funders Author Manuscripts

the oxidized [Mo_3] clusters evidenced by EPR spectroscopy. Based on this information, we tentatively assign the two pre-catalytic reduction processes to the reduction of $Mo^V(S_2)$ and $\{Mo^V{=}O / H^+\}$17 (**A** cluster) centers (equations 1 and 2 respectively) present within the as-prepared *a*-MoS_x material. The last reduction (equation 2) generates unsaturated catalytically-ready Mo^{IV} centers (resting state) for H_2 evolution (see below).

$$\mathrm{Mo^{V}\,(S_2)} + 1\mathrm{e}^- \rightarrow \mathrm{Mo^{IV}\,(S_2)} \quad \text{(equation 1)}$$

$$\left\{\mathrm{Mo^{V}{=}O/H^+}\right\}(\mathbf{A}\ \mathrm{cluster}) + 1\mathrm{e}^- + 1\mathrm{H}^+ \rightarrow \mathrm{Mo^{IV}} - + \mathrm{H_2O} \quad \text{(equation 2)}$$

Insights into the catalytic H_2 evolution cycle

Figure 4c shows that an increase of pH by one unit requires ~55 mV to be added to the applied potential $E_{appl.}$ to sustain the catalytic current at a constant value. The catalytic current is thus under the control of an electrochemical process (concerted or not) involving $1e^-$ and $1H^+$. In order to gain more insights into the catalytic H_2 evolution mechanism, we also measured the resonance Raman spectrum of *a*-MoS_x films being electrochemically equilibrated under turn-over conditions for H_2 evolution (Fig. 2a, *black trace*). The electrode was held at a constant potential of –0.71 V *vs.* NHE (corresponding to 300 mV overpotential for HER) for 1h in a pH 7 phosphate buffer solution (Methods section). During such a process, each Mo site turns over 1000 times on average. Four major changes are observed in the activated material as compared to the as-prepared material (Fig. 2a, *red trace*): (i) the signal assigned to bridging and shared disulfide significantly decreased; (ii) the signal attributed to terminal disulfide ligands completely disappeared, (iii) the signal assigned to sulfide ligand is modified and (iv) signals in the 800-950 cm^{-1} region corresponding to Mo=O vibrations considerably increased.

Build-up of the catalytically-ready species and electrochemical corrosion of *a*-MoS_x under reductive conditions

Observations (i) and (ii) clearly indicate that all disulfide ligands are reduced and/or eliminated under turn-over conditions. Removal of terminal disulfide ligands can change the geometry of the [Mo_3] cluster that causes a shift of the Mo_3–μ_3S vibration (observation (iii)). We note that these observations may seem in contrast with previous observations made by Kibsgaard et al. on drop-casted salts of isolated $[Mo_3S_{13}]^{2-}$ clusters after the recording of ten cyclic voltammograms.13 We nevertheless think that the longer equilibration conditions used in this study provide a better picture of the transformation processes at play during turn-over. Reductive activation of *a*-MoS_x thus results in a net loss of sulfur to form a material which is better described as MoS_{2+x}, in agreement with the stoichiometry previously reported for active *a*-MoS_x obtained via cathodic electrolysis or dynamic potential cycling from $[MoS_4]^{2-}$. 10

Europe PMC Funders Author Manuscripts

Europe PMC Funders Author Manuscripts

The two equations proposed below could account for the transformations involving shared and bridging disulfides:

$$\mathrm{Mo}\,(\mu-\mathrm{S}_2)\,\mathrm{Mo}+2\mathrm{e}^- \rightarrow \mathrm{Mo}(\mu-\mathrm{S})_2\mathrm{Mo} \quad \text{(equation 3)}$$

$$\mathrm{Mo}\,(\mu-\mathrm{S}_2)\,\mathrm{Mo}+2\mathrm{e}^-+\mathrm{xH}^+ \rightarrow \mathrm{Mo}(=\mathrm{S})_{2-\mathrm{x}}(\mathrm{SH})_{\mathrm{x}}+\mathrm{Mo}- \quad \text{(equation 4)}$$

Equation 3 is a chemically reversible process that can simply be reverted following air equilibration. It can nevertheless explain the modification of the Raman spectrum in the sulfide ligand region observed under turnover conditions. By contrast, the $2e^-$, $2H^+$ reduction process (equation 4) shortens the polymeric chain while creating unsaturated Mo^{IV} centers and $Mo^{IV}(=S)_{2-x}(SH)_x$ centers, as recently proposed by Lassale-Kaiser et al.25 This process is thus likely the cause of the electrochemical corrosion of *a*-MoS_x electrode under reductive potentials reported by Hu and coll.36 However, side-products resulting from this corrosion are incomplete $[Mo_3]$ clusters rather than $[MoS_4]^{2-}$ generated from equation 5 as proposed by Hu and coll.36 To support this hypothesis, chemical corrosion of *a*-MoS_x nanoparticles with 0.1 M sodium dithionite solution was monitored using UV-visible spectroscopy. The solution turned rapidly green with visible absorption at λ_{max} = 600 nm, assigned to soluble $[Mo_3S_4]^{4+}$ or $[Mo_3S_7]^{4+}$ cores,37,38 but lacking the characteristic $[MoS_4]^{2-}$ absorptions at λ_{max} = 465 and 325 nm (Supplementary Fig. S11).

$$\mathrm{MoS_3}+1/8\,\mathrm{S_8}+2\mathrm{e}^- \rightarrow [\mathrm{MoS_4}]^{2-} \quad \text{(equation 5)}$$

Catalytic H_2 evolution cycle

The increase of signals in the 800-950 cm^{-1} region in the Raman spectrum of samples equilibrated under turn-over conditions for H_2 evolution (Fig. 2a, black trace) links the formation of Mo=O centers to catalytic H_2 evolution. The latter conclusion was also confirmed by EPR measurements. The spectrum of a frozen *a*-MoS_x suspension in pH 7 phosphate buffer was recorded under turn-over conditions induced by the addition of 0.14 M sodium dithionite. By comparison to the spectrum of the as-prepared state, two very intense signals (corresponding spectrum is shown in Fig. 2d, *black trace*, after ten-fold downscaling) are observed. The first one corresponds to Mo^V=O centers massively produced under turn-over conditions, an observation consistent with resonance Raman studies. A second very broad transition is observed at g = 2.08, the intensity of which strongly increases when the temperature decreases from 77 K to 10 K (Supplementary Fig. S12). We relate this signal to a catalytic Mo^V intermediate which accumulates in solution under turn-over conditions.

We propose in Fig. 5 a catalytic cycle for H_2 evolution, consistent with all the above observations. The catalytically-ready species are unsaturated Mo^{IV} sites as evidenced by the disappearance of disulfide $\bar{\nu}$(S-S) signals in resonance Raman spectra. Such unsaturated Mo^{IV} sites are formed during the pre-catalytic peaks corresponding to the activation of

Europe PMC Funders Author Manuscripts

Europe PMC Funders Author Manuscripts

defect [Mo_3] clusters (equation 2) which is fully achieved at the potential of the catalytic process. Reduction of bridging disulfide ligands (equation 4) and elimination of terminal disulfide ligands, either as stepwise or concerted processes (equation 6), also partake in the formation of unsaturated Mo^{IV} sites.

$$\mathrm{Mo\,(S_2)} + 2e^- + 2H^+ \rightarrow \mathrm{Mo} - + HS^- \quad \text{(equation 6)}$$

From unsaturated Mo^{IV} sites, proton-coupled reduction of this species then generates the active species. This is in line with the pH dependence of the catalytic current (Fig 4c). Generation of unsaturated Mo^{IV} sites from equation 6, at potentials close to that of the catalytic H_2 evolution process and with the same dependence on pH, can also act as the rate-determining step during the initial electrochemical equilibration of the material.

From the active species, H_2 is evolved either in a homolytic way or upon protonation (heterolytic route), generating unsaturated Mo^V in the latter case. Hydration of such species would yield Mo^V=O centers, thus providing an explanation for accumulation of such species in the medium. We note that such a process is chemically reversible and controlled by the pH of the solution.

The above mentioned mechanism is quite similar to the one already proposed to occur at the edge-plane of *c*-$MoS_2$23,25 in terms of alternate electron and proton transfer steps. However our data definitively show that terminal disulfide ligands are fully displaced under catalytic turnovers which forced us to reinvestigate the structure of the active species. Using the same methodology as mentioned above, we calculated the structural, electronic and magnetic properties of possible catalytic models (**B** and **C** clusters) shown in Fig. 6 resulting from the addition of $1e^-$ and $1H^+$ to the unsaturated Mo^{IV} resting state. It followed that a Mo^V-hydride species is stabilized by 18 kcal.mol^{-1} compared to its isomer in which H atom addition takes place at a bridging disulfide ligand. The computed magnetic properties (Supplementary Tables S1 and S2) of such a metal-centered paramagnetic species are in agreement with the broad signal at g = 2.07 observed under turnover conditions for *a*-MoS_x, while the sulfur-based radical species **C** should exhibit EPR parameters close to the Landé factor (g = 2.0023). Not surprisingly, protonation of both species and generation of H_2 at pH 7 was found to be energetically favourable by 67 and 100 kJ.mol^{-1}, respectively (Supplementary Table S3). Using the methodology developed by Nørskov,23 we calculated the H atom adsorption free energies (ΔG^0_H) corresponding to generation of the Mo^V-hydride species **B** (0. 108 eV) and to the sulfur-based radical **C** (0.44 eV) from the Mo^{IV} resting state (Supplementary Table S4). It is well known that ΔG^0_H values close to zero characterize efficient catalytic HER material, which further favors the mechanistic route through the Mo^V-hydride intermediate. The quite high ΔG^0_H value obtained for intermediate **C** is in full agreement with the value determined for a similar {Mo_3S_4} cluster with H atom addition on a sulfur center.21 By contrast, the low ΔG^0_H value calculated for the process involving the Mo^V–hydride **B** in *a*–MoS_x is comparable to the reported ΔG^0_H value (0.08 eV) for *c*–MoS_2, thus in full agreement with the good HER activities of both amorphous and crystalline materials.23 We finally note that, in the course of the revision process of this manuscript,

Europe PMC Funders Author Manuscripts

Europe PMC Funders Author Manuscripts

DFT studies concluded to the involvement of a Mo-bound hydride species as the active species in H_2 evolution catalysed by MoS_2.39,40

Conclusion

In this report, we have revealed the polymeric structure and molecular nature of amorphous molybdenum sulfide which can now be formulated as a coordination polymer based on $[Mo_3S_{13}]^{2-}$ clusters sharing disulfide ligands. This specific structure has many implications on the reactivity of the material as compared to its crystalline analogues. A first one is the possibility for cathodic corrosion leading to a shortening of the polymeric chains under electrochemical activation. In addition, under turnover H_2 generation conditions, elimination of terminal disulfide ligands generates the actual catalytic centers for proton reduction, which hydrates and generates molybdenum oxysulfide sites. Such findings may also be relevant for the understanding of the chemical reactivity of similar transition metal dichalcogenide materials41 used as catalysts42–44 or in electrochemical storage devices.45 More broadly, this study provides another example of the duality between crystalline and amorphous materials regarding catalytic properties. Previous examples including manganese46,47 and cobalt oxide-based48–50 catalysts for water oxidation have shown that amorphous materials' superior activities go beyond an increased surface area, but are intimately linked to distinct structure and nature of catalytically active sites, as shown here for the first time for a H_2-evolving material. Based on such structural and mechanistic understanding, proton–electron transport and transfer studies in *a*-MoS_x electrocatalytic films are now conceivable. Solutions to avoid or control reductive corrosion of *a*-MoS_x materials can also be developed, together with rational optimization of their catalytic performances, through synthetic modifications of the cluster units and/or the connecting ligands.

Methods

Ammonium tetrathiomolybdate $[MoS_4](NH_4)_2$ and other chemicals were purchased from Sigma Aldrich and used as-received without any further purification. Fluorine–doped tin oxide (FTO) coated glass slides with 14 Ω/sq resistivity and a thickness of 400 nm were purchased from NSG group. FTO electrode was cleaned by subsequent sonication in acetone, isopropanol and ethanol and then dried by a nitrogen gas flux before used.

Electrochemical experiments were performed on an Autolab PGSTAT-30 potentiostat employing a conventional three electrodes configuration. Customized two compartment electrochemical cell was used. The working electrode was the synthesized catalyst film on 1 cm^2 FTO or 0.071 cm^2 carbon glassy electrode. Reference electrode was an Ag/AgCl 3M KCl while counter electrode was a Pt wire. Reference electrode was calibrated daily by employing a solution of $[Fe(CN)_6]^{3-}/[Fe(CN)_6]^{4-}$ in pH 7 potassium phosphate buffer.

Potentials are quoted against the *Normal Hydrogen Electrode* (NHE), by using the following equation:

$$E_{vs.\ \mathrm{NHE}} = E_{vs.\ \mathrm{Ag/AgCl}} + 0.21\ \mathrm{V}$$

Europe PMC Funders Author Manuscripts

Europe PMC Funders Author Manuscripts

Electrolytes employed were 0.5 M H_2SO_4 (pH 0), 0.5 M buffered citrate solution (pH 2 – 4), 0.5 M buffered phosphate solution (pH 6 – 8); and 0.5 M buffered borate solution (pH 9 – 11). Prior to use, electrolyte solution was saturated with N_2 gas.

Raman analysis was conducted on a NRS-7100 Laser Raman Spectrometer (JASCO, Japan) using a 532 nm green line laser. Prior to measurement, wavelength calibration was done using the bulk Si peak at 520 cm^{-1} as standard reference. *In situ a*-MoS_x to c-MoS_2 crystallization readily occurred when high laser power (1.2 mW) was used. To avoid the crystallization of $(Mo_3S_{11})_n$ polymer induced by the laser source, very low power of 0.1 mW was employed. Exposed time was 480 seconds and a 100X objective lens was used.

X-ray photoelectron spectroscopy (XPS) measurements were carried using a Thermo Scientific Theta Probe system (VG ESCALAB 220i–XL instrument) equipped with a monochromatic Al k_α(1486.6 eV) X ray source. The photoelectrons signals were collected in the constant pass energy mode using a concentric hemispherical energy analyser that was calibrated with pure gold, silver, and copper standard samples by setting the Au $4f_{7/2}$, Ag $3d_{5/2}$, and Cu $2p_{3/2}$ peaks at binding energies of 83.96 ± 0.02 eV, 368.21 ± 0.02 eV, and 932.62 ± 0.02 eV, respectively. Charge referencing was corrected using the adventitious hydrocarbon at binding energy of 284.6 eV. Quantitative analysis of the XPS spectra was carried out using a Shirley background subtraction before performing a least-square-error fit with a mixture of Gaussian and Lorentzian line shapes. The spin–orbit split peaks for S 2p is constrained using a separation of 1.18 eV with a ratio of ~0.5 while that of the Mo 3d was constrained using a separation of 3.13 eV with a ratio of 0.67. All the corresponding spin-orbit split peaks were set to have the same FWHM and similar line shapes.

X-band EPR spectra were obtained using a Bruker EMX spectrometer equipped with an Oxford ESR 910 cryostat for low temperature studies. The microwave frequency was calibrated with a frequency counter and the magnetic field with an NMR gaussmeter.

Elemental analysis were performed using ICP-AES at the Laboratory of Chemistry and Biology of Metals (Grenoble) and at the Institut des Sciences Analytiques (CNRS, Villeurbanne, France).

1. Preparation of *a*-MoS_x thin film

a-MoS_x thin films were grown by holding FTO (14 Ω/sq resistivity) or glassy carbon disk electrode at an anodic potential of 0.2 or 0.5 V *vs.* NHE in a deposition bath consisting of 1.0 mM $[MoS_4](NH_4)_2$ in degassed pH 7 phosphate buffer. During deposition, the solution was stirred with aid of a magnetic stirrer. Total density of charges of 12 $mC.cm^{-2}$ was passed through working electrode resulting in the deposition of 6.2×10^{-8} mol Mo catalyst. When the resulting film was formed, it was intensively washed with degassed water and ethanol, followed by drying under a stream of argon. The films were kept in a gas-tight closed glass tube filled with argon gas.

In a separate experiment, 0.2 mM $MnCl_2$ was added to the deposition bath together with 1.0 mM $[MoS_4](NH_4)_2$. At 0.2 V *vs.* NHE, the film obtained from this deposition showed

identical XPS signatures to those recorded for films grown without $MnCl_2$ added. XPS analysis did not reveal incorporation of Mn^{2+} or Cl^- within the deposited film.

2. Preparation of *a*-MoS_x nanoparticles via chemical oxidation of $[MoS_4](NH_4)_2$

Sodium persulfate (2 mmol, 480 mg) was added to a deep-red solution of $[MoS_4](NH_4)_2$ (1 mmol, 260 mg) in water (50mL) well gased with Ar. The solution rapidly turned to dark brown suspension which was continuously stirred under Ar for 2 h. When the reaction was over, dark brown powder was collected by centrifugation, intensively washed with water, ethanol, CS_2 and diethyl ether. This product was dried under an Ar stream and kept under Ar atmosphere.

3. Extrusion of $[Mo_3S_{13}](Et_4N)_2$ from *a*-MoS_x

a-MoS_x nanoparticles (325 mg, 0.51 mmol (Mo_3S_{11}) monomer) were loaded into a 5% KOH solution (5 mL) well-degased with Ar. The resulting orange suspension was continuously stirred overnight under Ar. It was then centrifuged, giving a red solution and orange precipitates. These precipitates were washed with water (2 × 2.5 mL) giving an orange washing solution, which was then combined together with the above red solution. To this final solution was added excess Et_4NBr (~0.5 g) resulting in rapid precipitation of a red powder which was then collected by centrifugation, washed intensively with water until obtaining colourless washing solution. Finally, the obtained red powder was washed with 2 × 5 mL ethanol, 2 × 5 mL diethyl ether and dried under vacuum overnight giving $[Mo_3S_{13}](Et_4N)_2$ as a red product (65 mg, 0.067 mmol, yield ~13%). This material was soluble in DMF or DMSO solvents.

4. Conditioning *a*-MoS_x catalyst under pre-waves or H_2 evolution conditions

a-MoS_x electrodes deposited on FTO substrate (loading of 6.2×10^{-8} mol cm^{-2}) were equilibrated in a thoroughly degased pH 7 phosphate buffer solution for 1h at pre-wave potentials (–0.45 or –0.55 V *vs.* NHE) or at catalytic H_2-evolving potential (–0.71 V *vs.* NHE). After equilibration, the samples were carefully rinsed with O_2-free deionized water, dried under Ar and quickly transferred to Raman and XPS spectrometers. The samples were kept under Ar during the transfer and loading time.

In an Ar-filled glove box, a suspension of *a*-MoS_x nanoparticles in pH7 phosphate buffer solution (2 mg. mL^{-1}) was prepared. To this suspension, 0.14M sodium dithionite was added. After short equilibration time at room temperature, the sample was frozen and transferred to EPR spectrometer for measurement. In a separated experiment employing identical conditions, H_2 evolution was probed employing a miniaturized Clark electrode (Unisense H_2 sensor in guide and monometer).

Supplementary Material

Refer to Web version on PubMed Central for supplementary material.

Europe PMC Funders Author Manuscripts
Europe PMC Funders Author Manuscripts

Europe PMC Funders Author Manuscripts

Europe PMC Funders Author Manuscripts

Acknowledgements

P. D. Tran and J. Barber acknowledge the Energy Research Institute @ Nanyang Technological University (ERI@N) and the Singapore-Berkeley Research Initiative for Sustainable Energy (SinBeRISE) CREATE for financial and facilities supports. P. D. Tran acknowledges University of Science and Technology of Hanoi for startup funding support (project USTH PECH2). Q. D. Truong and I. Honma acknowledge the Japan Society for Promotion of Science for financial support (Grant No. P13070). This work was supported by the French National Research Agency (Labex program, ARCANE, ANR-11-LABX-0003-01) and the European Research Council under the European Union's Seventh Framework Programme (FP/2007-2013)/ERC Grant Agreement n.306398. Dr J. Pérard is gratefully acknowledged for his help during ICP-AES measurements.

References and Notes

1. McKone JR, Lewis NS, Gray HB. Will Solar-Driven Water-Splitting Devices See the Light of Day? Chem Mater. 2014; 26:407–414.
2. Le Goff A, et al. From hydrogenases to noble metal-free catalytic nanomaterials for H2 production and uptake. Science. 2009; 326:1384–1387. [PubMed: 19965754]
3. Huan TN, et al. Bio-inspired noble metal-free nanomaterials approaching platinum performances for H2 evolution and uptake. Energy Environ Sci. 2016; doi: 10.1039/C5EE02739J
4. McKone JR, Marinescu SC, Brunschwig BS, Winkler JR, Gray HB. Earth-abundant hydrogen evolution electrocatalysts. Chem Sci. 2014; 5:865–878.
5. Andreiadis ES, et al. Molecular engineering of a cobalt-based electrocatalytic nanomaterial for H2 evolution under fully aqueous conditions. Nature Chem. 2013; 5:48–53. [PubMed: 23247177]
6. Jaramillo TF, et al. Identification of active edge sites for electrochemical H2 evolution from MoS2 nanocatalysts. Science. 2007; 317:100–102. [PubMed: 17615351]
7. Kibsgaard J, Chen Z, Reinecke BN, Jaramillo TF. Engineering the surface structure of MoS2 to preferentially expose active edge sites for electrocatalysis. Nature materials. 2012; 11:963–969. [PubMed: 23042413]
8. Kong D, et al. Synthesis of MoS2 and MoSe2 Films with Vertically Aligned Layers. Nano Lett. 2013; 13:1341–1347. [PubMed: 23387444]
9. Lukowski MA, et al. Enhanced hydrogen evolution catalysis from chemically exfoliated metallic MoS2 nanosheets. J Am Chem Soc. 2013; 135:10274–10277. [PubMed: 23790049]
10. Morales-Guio CG, Hu X. Amorphous Molybdenum Sulfides as Hydrogen Evolution Catalysts. Acc Chem Res. 2014; 47:2671–2681. [PubMed: 25065612]
11. Benck JD, Chen Z, Kuritzky LY, Forman AJ, Jaramillo TF. Amorphous Molybdenum Sulfide Catalysts for Electrochemical Hydrogen Production: Insights into the Origin of their Catalytic Activity. ACS Catal. 2012; 2:1916–1923.
12. Jaramillo TF, et al. Hydrogen Evolution on Supported Incomplete Cubane-type [Mo3S4]4+ Electrocatalysts. J Phys Chem C. 2008; 112:17492–17498.
13. Kibsgaard J, Jaramillo TF, Besenbacher F. Building an appropriate active-site motif into a hydrogen-evolution catalyst with thiomolybdate [Mo3S13]2− clusters. Nature Chem. 2014; 6:248–253. [PubMed: 24557141]
14. Merki D, Fierro S, Vrubel H, Hu X. Amorphous Molybdenum Sulfide Films as Catalysts for Electrochemical Hydrogen Production in Water. Chem Sci. 2011; 2:1262–1267.
15. Voiry D, et al. Enhanced Catalytic Activity in Strained Chemically Exfoliated WS2 Nanosheets for Hydrogen Evolution. Nature materials. 2013; 12:850–855. [PubMed: 23832127]
16. Tran PD, et al. Novel Cobalt/Nickel–Tungsten-Sulfide Catalysts for Electrocatalytic Hydrogen Generation from Water. Energy Environ Sci. 2013; 6:2452–2459.
17. Huang Z, et al. Dimeric [Mo2S12]2− Cluster: A Molecular Analogue of MoS2 Edges for Superior Hydrogen-Evolution Electrocatalysis. Angew Chem Int Ed. 2015; 54:15181–15185. DOI: 10.1002/anie.201507529
18. Tran PD, et al. Novel Assembly of an MoS2 Electrocatalyst onto a Silicon Nanowire Array Electrode to Construct a Photocathode Composed of Elements Abundant on the Earth for Hydrogen Generation. Eur J Chem. 2012; 18:13994–13999.

Europe PMC Funders Author Manuscripts

Europe PMC Funders Author Manuscripts

19. Seger B, et al. Hydrogen Production Using a Molybdenum Sulfide Catalyst on a Titanium-Protected n+p-Silicon Photocathode. Angew Chem Int Ed. 2012; 51:9128–9131.
20. Morales-Guio CG, Tilley SD, Vrubel H, Gratzel M, Hu X. Hydrogen evolution from a copper(I) oxide photocathode coated with an amorphous molybdenum sulphide catalyst. Nature Commun. 2014; 5:3059. [PubMed: 24402352]
21. Hou Y, et al. Bioinspired Molecular Co-Catalysts Bonded to a Silicon Photocathode for Solar Hydrogen Evolution. Nature materials. 2011; 10:434–438. [PubMed: 21516095]
22. Bourgeteau T, et al. A H2-evolving photocathode based on direct sensitization of MoS3 with an organic photovoltaic cell. Energy Environ Sci. 2013; 6:2706–2713.
23. Hinnemann B, et al. Biomimetic Hydrogen Evolution: MoS2 Nanoparticles as Catalyst for Hydrogen Evolution. J Am Chem Soc. 2005; 127:5308–5309. [PubMed: 15826154]
24. Lauritsen JV, et al. Size-dependent structure of MoS2 nanocrystals. Nature nanotechnology. 2007; 2:53–58. DOI: 10.1038/nnano.2006.171
25. Lassalle-Kaiser B, et al. Evidence from in Situ X-ray Absorption Spectroscopy for the Involvement of Terminal Disulfide in the Reduction of Protons by an Amorphous Molybdenum Sulfide Electrocatalyst. J Am Chem Soc. 2015; 137:314–321. [PubMed: 25427231]
26. Bélanger D, Laperriére G, Marsan B. The electrodeposition of amorphous molybdenum sulfide. J Electroanal Chem. 1993; 347:165–183.
27. Müller A, Wittneben V, Krickemeyer E, Bögge H, Lemke M. Studies on the triangular cluster [Mo3S13]2−: Electronic structure (Xα calculations, XPS), crystal structure of (Ph4As)2[Mo3S13]. 2CH3CN and a refinement of the crystal structure of (NH4)2[Mo3s13]·H2O. Zeitschrift für anorganische und allgemeine Chemie. 1991; 605:175–188. DOI: 10.1002/zaac.19916050121
28. Muller A, Fedin V, Hegetschweiler K, Amrein W. Characterization of amorphous substances by studying isotopically labelled compounds with FAB-MS: evidence for extrusion of triangular Mo3 clusters from a mixture of 92MoS3 and 100MoS3 by reaction with OH. J Chem Soc Chem Commun. 1992:1795–1796.
29. Weber T, Muijsers JC, van Wolput JHMC, Verhagen CPJ, Niemantsverdriet JW. Basic Reaction Steps in the Sulfidation of Crystalline MoO3 to MoS2, As Studied by X-ray Photoelectron and Infrared Emission Spectroscopy. J Phys Chem. 1996; 100:14144–14150.
30. Benoist L, et al. X-ray photoelectron spectroscopy characterization of amorphous molybdenum oxysulfide thin films. Thin Solid Films. 1995; 258:110–114. DOI: 10.1016/0040-6090(94)06383-4
31. Chiam SY, et al. Investigating the stability of defects in MoO3 and its role in organic solar cells. Sol Energy Mater Sol Cells. 2012; 99:197–203.
32. Okamura, T-a, Tatsumi, M., Omi, Y., Yamamoto, H., Onitsuka, K. Selective and Effective Stabilization of MoVI═O Bonds by NH···S Hydrogen Bonds via Trans Influence. Inorg Chem. 2012; 51:11688–11697. [PubMed: 23075211]
33. Dessapt R, et al. Novel Mo(V)-Dithiolene Compounds: Characterization of Nonsymmetric Dithiolene Complexes by Electrospray Ionization Mass Spectrometry. Inorg Chem. 2003; 42:6425–6431. [PubMed: 14514318]
34. Sugimoto H, et al. Oxo-sulfido- and oxo-selenido-molybdenum(vi) complexes possessing a dithiolene ligand related to the active sites of hydroxylases of molybdoenzymes: low temperature preparation and characterisation. Chem Commun. 2013; 49:4358–4360.
35. Busetto L, Vaccari A, Martini G. Electron spin resonance of paramagnetic species as a tool for studying the thermal decomposition of molybdenum trisulfide. J Phys Chem. 1981; 85:1927–1930.
36. Vrubel H, Hu X. Growth and Activation of an Amorphous Molybdenum Sulfide Hydrogen Evolving Catalyst. ACS Catal. 2013; 3:2002–2011.
37. Shibahara T, et al. Syntheses and electrochemistry of incomplete cubane-type clusters with M3S4 cores (M = molybdenum, tungsten). X-ray structures of [W3S4(H2O)9](CH3C6H4SO3)4.cntdot.9H2O, Na2[W3S4(Hnta)3].cntdot.5H2O, and (bpyH)5[W3S4(NCS)9].cntdot.3H2O. Inorg Chem. 1992; 31:640–647.
38. Weber T, Muijsers JC, Niemantsverdriet JW. Structure of Amorphous MoS3. J Phys Chem. 1995; 99:9194–9200.

Europe PMC Funders Author Manuscripts

Europe PMC Funders Author Manuscripts

39. Huang Y, Nielsen RJ, Goddard WA, Soriaga MP. The Reaction Mechanism with Free Energy Barriers for Electrochemical Dihydrogen Evolution on MoS2. J Am Chem Soc. 2015; 137:6692–6698. [PubMed: 25941943]
40. Li H, et al. Activating and optimizing MoS2 basal planes for hydrogen evolution through the formation of strained sulphur vacancies. Nature materials. 2016; 15:48–53. DOI: 10.1038/nmat4465 [PubMed: 26552057]
41. Gibney E. The super materials that could trump graphene. Nature. 2015; 522:274–276. [PubMed: 26085254]
42. Zhang X, et al. Amorphous MoSxCly electrocatalyst supported by vertical graphene for efficient electrochemical and photoelectrochemical hydrogen generation. Energy Environ Sci. 2015; 8:862–868.
43. Kornienko N, et al. Operando Spectroscopic Analysis of an Amorphous Cobalt Sulfide Hydrogen Evolution Electrocatalyst. J Am Chem Soc. 2015; 137:7448–7455. [PubMed: 26051104]
44. Caban-Acevedo M, et al. Efficient hydrogen evolution catalysis using ternary pyrite-type cobalt phosphosulphide. Nature materials. 2015; 14:1245–1251. [PubMed: 26366849]
45. Hu X, Zhang W, Liu X, Mei Y, Huang Y. Nanostructured Mo-based electrode materials for electrochemical energy storage. Chem Soc Rev. 2015; 44:2376–2404. [PubMed: 25688809]
46. Zaharieva I, et al. Synthetic manganese-calcium oxides mimic the water-oxidizing complex of photosynthesis functionally and structurally. Energy Environ Sci. 2011; 4:2400–2408.
47. Huynh M, Bediako DK, Nocera DG. A Functionally Stable Manganese Oxide Oxygen Evolution Catalyst in Acid. J Am Chem Soc. 2014; 136:6002–6010. [PubMed: 24669981]
48. Kanan MW, Surendranath Y, Nocera DG. Cobalt-phosphate oxygen-evolving compound. Chem Soc Rev. 2009; 38:109–114. [PubMed: 19088970]
49. Shevchenko D, Anderlund MF, Thapper A, Styring S. Photochemical water oxidation with visible light using a cobalt containing catalyst. Energy Environ Sci. 2011; 4:1284–1287.
50. Hutchings GS, et al. In Situ Formation of Cobalt Oxide Nanocubanes as Efficient Oxygen Evolution Catalysts. J Am Chem Soc. 2015; 137:4223–4229. [PubMed: 25759959]

Europe PMC Funders Author Manuscripts

Europe PMC Funders Author Manuscripts

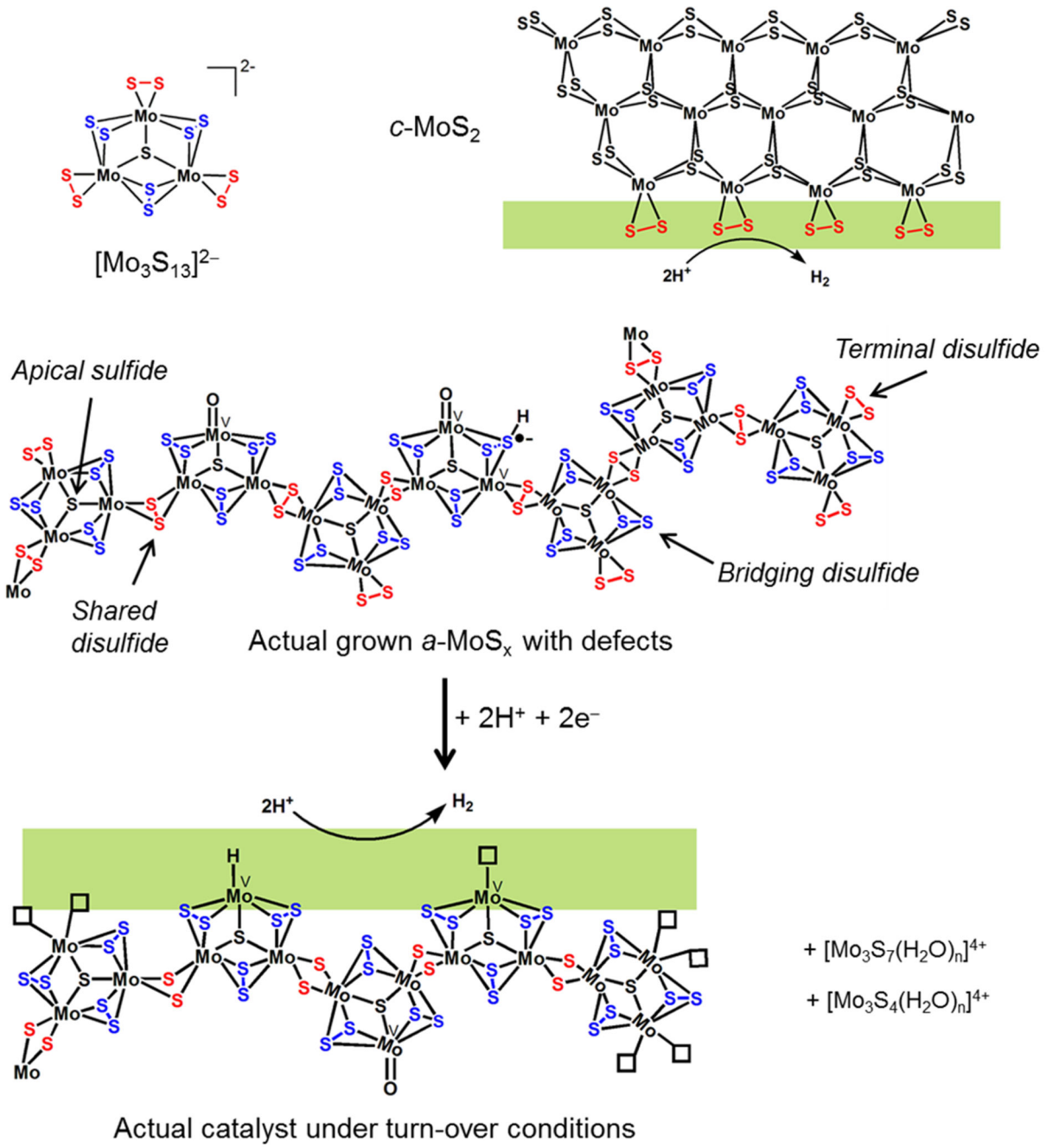

Figure 1. Structures of molybdenum sulfide materials.

$[Mo_3S_{13}]^{2-}$ cluster; c-MoS_2 wherein Mo edge plan contains $Mo(S_2)$ catalytic active sites; Actual *a*-MoS_x coordination polymer with $[Mo_3S_{13}]^{2-}$ building block units sharing two of their three terminal disulfide bond to form polymeric chain. Some defect Mo^V=O sites are present within the polymer; The same *a*-MoS_x catalyst under catalytic H_2 evolution turnover conditions. Within *a*-MoS_x, four different ligands are thus identified: apical sulfide μ-S^{2-}, bridging disulfides $(S\text{-}S)^{2-}{}_{br}$, shared $(S\text{-}S)^{2-}{}_{sh}$ and terminal disulfides $(S\text{-}S)^{2-}{}_{t}$.

Europe PMC Funders Author Manuscripts

Europe PMC Funders Author Manuscripts

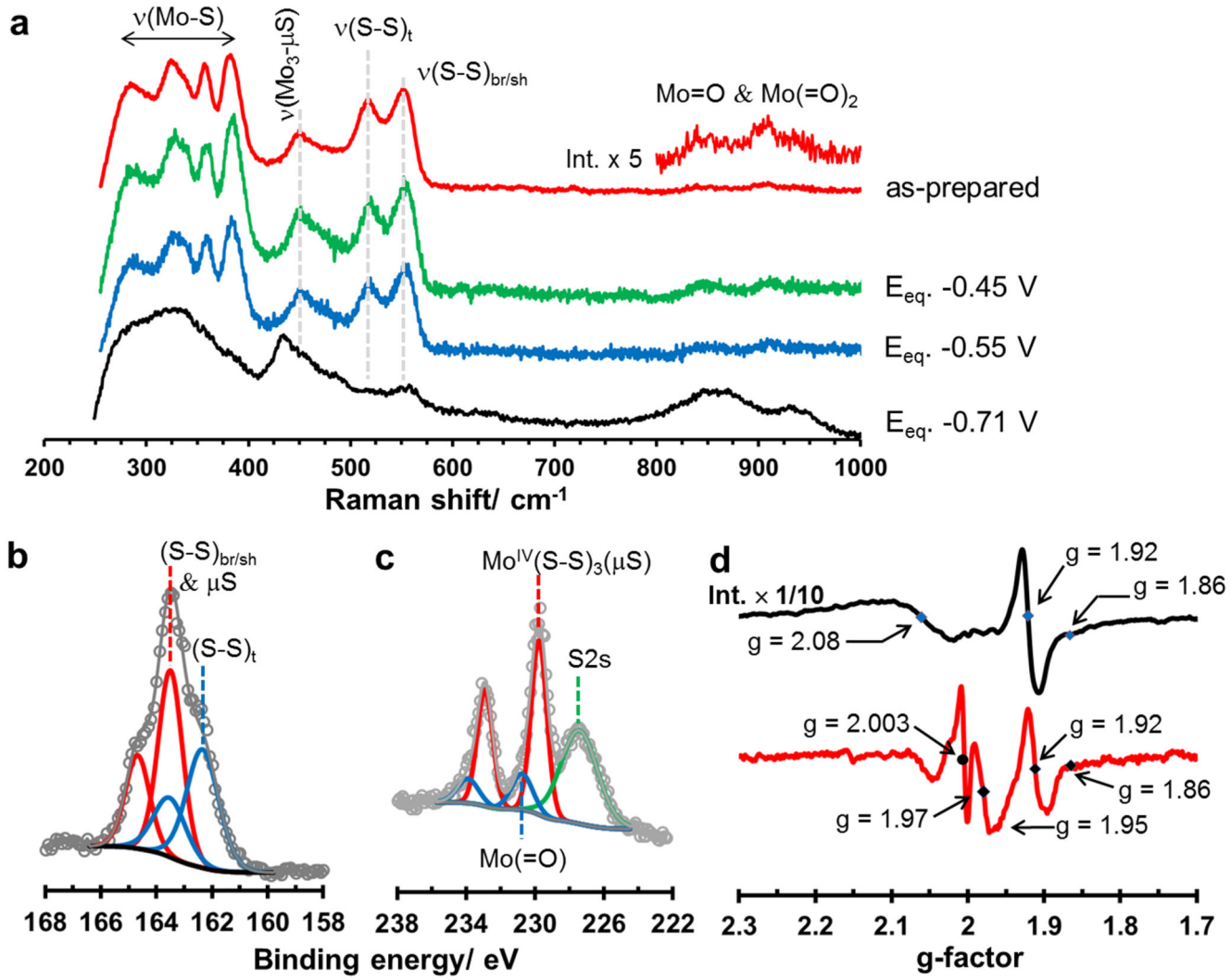

Figure 2. Spectroscopic characterization of *a*-MoS_x catalyst.

a, Resonance Raman spectra (532 nm green laser excitation with low power 0.1 mW); red trace: freshly electrodeposited *a*-MoS_x thin film (red trace insert: zoom up Mo=O vibration bands by multiplying intensity by factor 5); the same material after equilibration in pH 7 phosphate solution at constant potential of -0.45 V (green trace), -0.55 V (blue trace) and -0.71 V vs. NHE (black trace). **b** and **c,** XPS core-level spectra and deconvolutions into S 2p and Mo 3d contributions for a freshly electrodeposited *a*-MoS_x thin film. **d,** EPR spectrum measured on as-prepared *a*-MoS_x nanoparticles in frozen pH 7 phosphate buffer suspension (2 mg. mL^{-1}) at 77 K (red trace) and after treated with 0.14 M sodium dithionite (black trace, intensity is devised by 10).

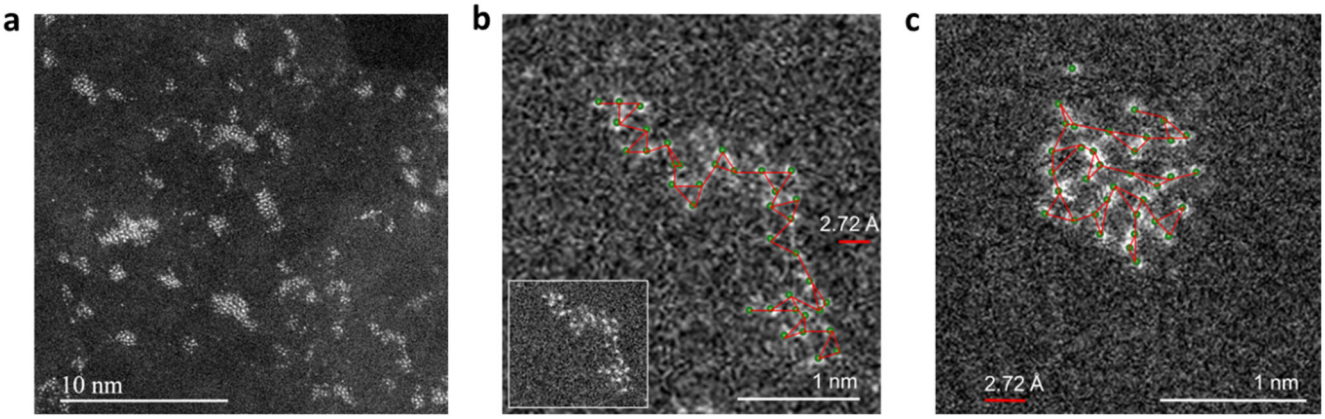

Figure 3. HAADF-STEM analysis.

a, low resolution shows well-isolated sub-nano and nanoparticles. **b** and **c**, arrangement of [Mo_3] cluster units in an one-dimensional unfolding chain and two-dimensional branched structure.

Europe PMC Funders Author Manuscripts

Europe PMC Funders Author Manuscripts

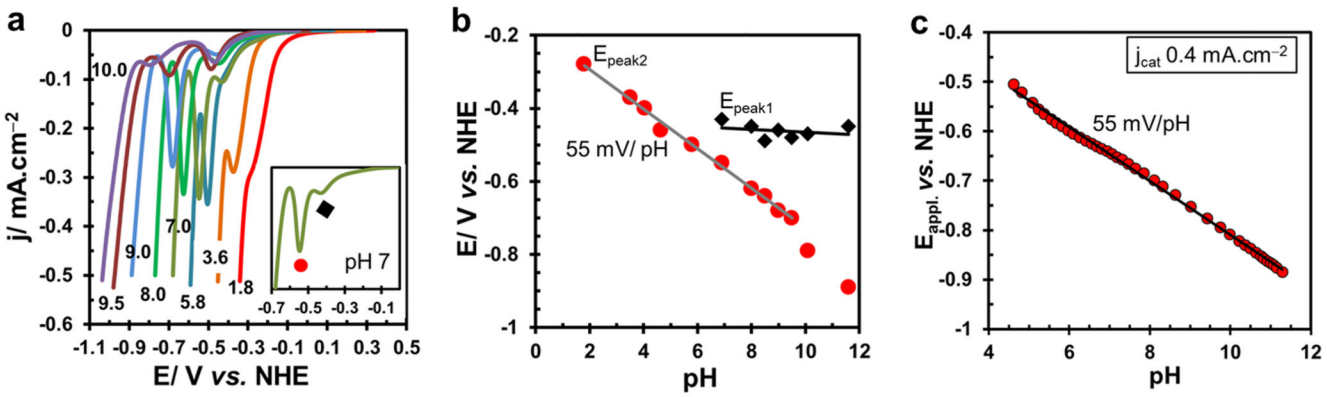

Figure 4. Electrochemical properties of *a*-MoS_x electrode.

a, the first potential polarization curves recorded in different pH electrolyte solutions (insert: the curve obtained in pH 7 solution) on an *a*-MoS_x electrode (catalyst loading of 6.2×10^{-8} mole.cm^{-2}), freshly grown by electrodeposition at 0.2 V vs. NHE; Potential scan rate was 2 mV.s^{-1}; **b,** dependence of peak potential of the pre-catalytic reduction events on the pH of the electrolyte solution; **c**, pH titration employing an *a*-MoS_x electrode grown on glassy carbon disk to sustain a catalytic current of 0.4mA.cm^{-2}. Carbon disk was rotated at 1000 rpm.

Europe PMC Funders Author Manuscripts
Europe PMC Funders Author Manuscripts

Europe PMC Funders Author Manuscripts

Europe PMC Funders Author Manuscripts

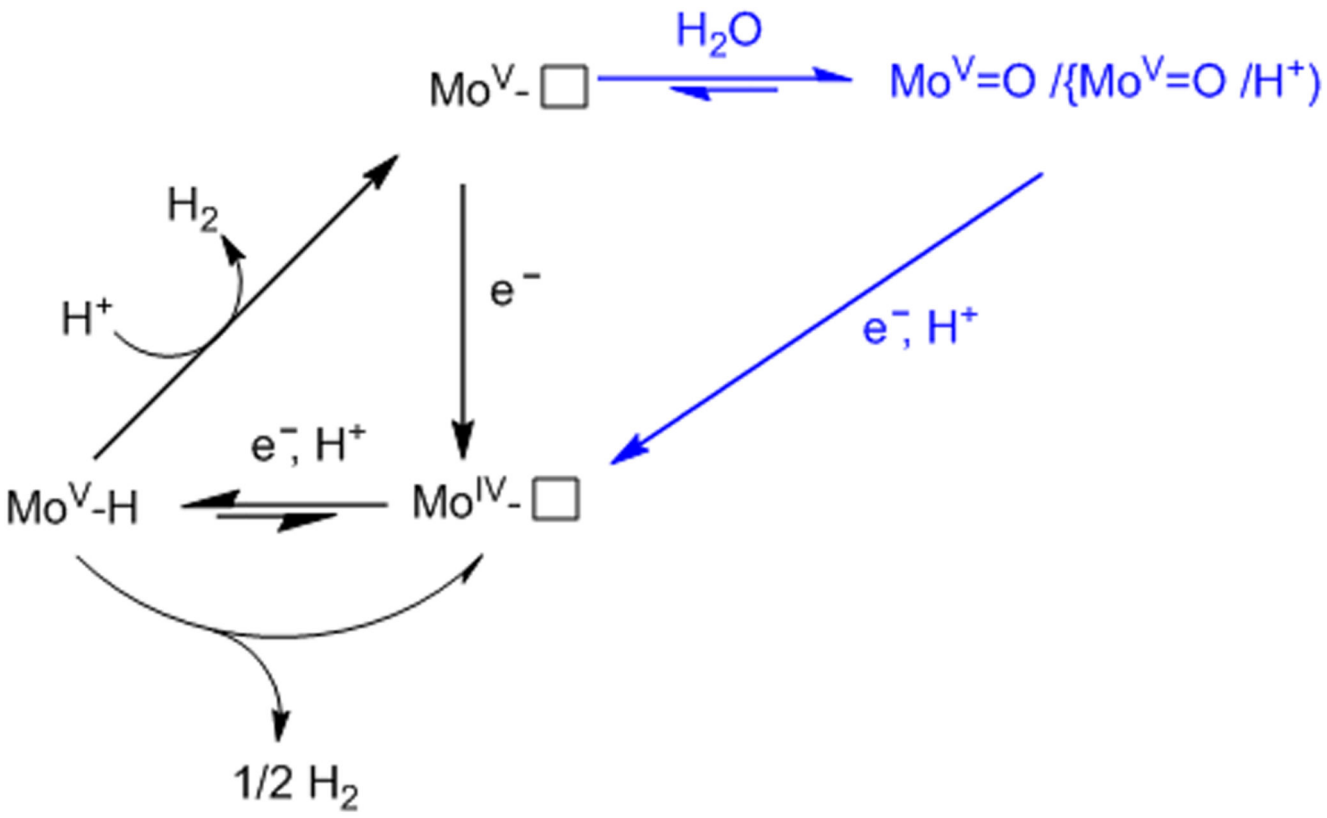

Figure 5. Proposed catalytic pathway for H_2 evolution

(equations 4 and 6 are not included in this scheme but contribute to the formation of the unsaturated Mo^{IV} sites)

Europe PMC Funders Author Manuscripts

Europe PMC Funders Author Manuscripts

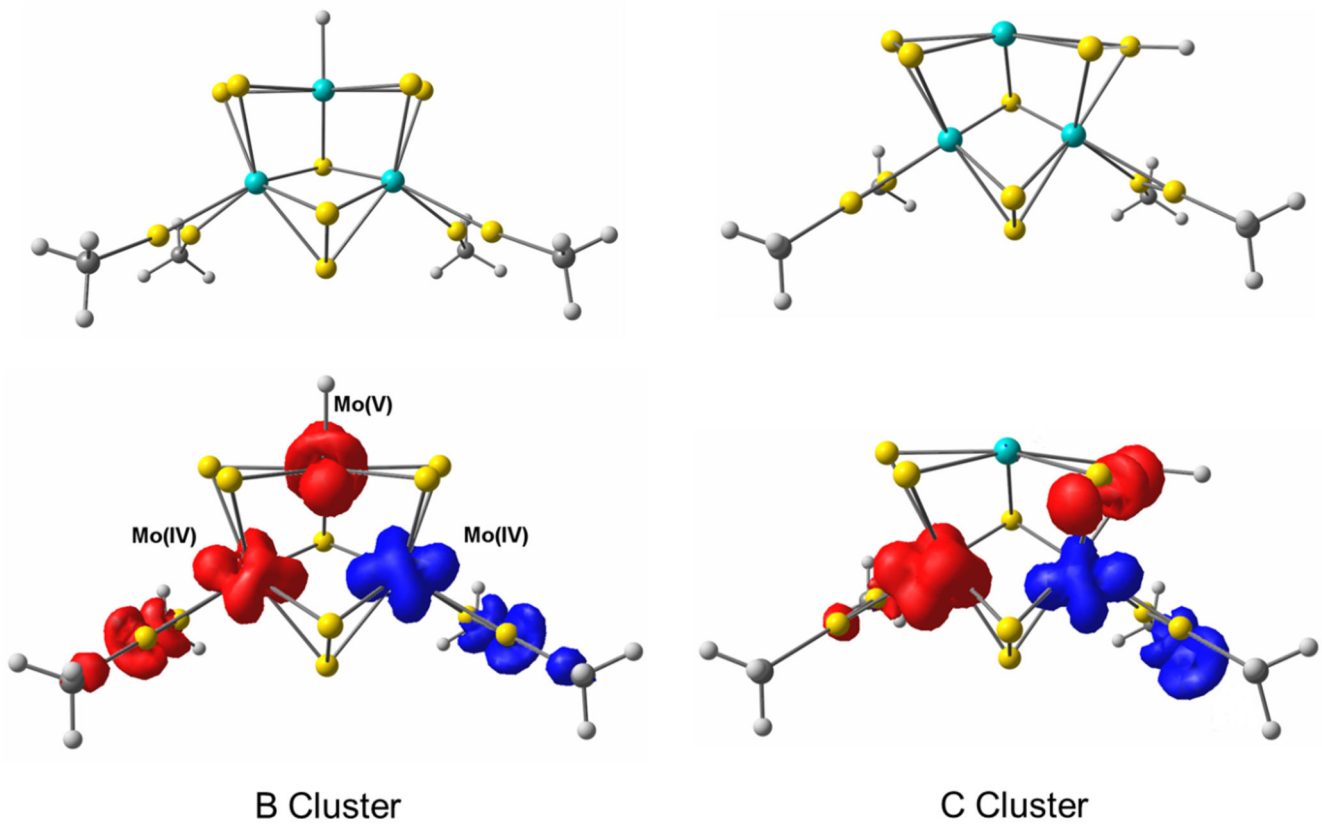

Figure 6.

Truncated models (starting state for DFT calculations) of two isomeric **B** (left) and **C** (right) clusters corresponding to the catalytically active state and their spin distributions. Positive and negative populations are depicted in red and blue, respectively (See Supplementary Tables S1 and 2).